A comparison of second- and sixth-order methods for large-eddy simulations

M. Meinke *, W. Schröder, E. Krause, Th. Rister

Aerodynamisches Institut, RWTH Aachen, Wüllnerstr. zw. 5 u. 7, 52062 Aachen, Germany

Abstract

Large-eddy simulations of spatially developing planar turbulent jets are performed using a compact finite-difference scheme of sixth-order and an advective upstream splitting method-based method of second-order accuracy. The applicability of these solution schemes with different subgrid scale models and their performance for realistic turbulent flow problems are investigated. Solutions of the turbulent channel flow are used as an inflow condition for the turbulent jets. The results compare well with each other and with analytical and experimental data. For both solution schemes, however, the influence of the subgrid scale model on the time averaged turbulence statistics is small. This is known to be the case for upwind schemes with a dissipative truncation error, but here it is also observed for the high-order compact scheme. The reason is found to be the application of a compact high-frequency filter, which has to be used with strongly stretched computational grids to suppress high-frequency oscillations. The comparison of the results of the two schemes shows hardly any difference in the quality of the solutions. The second-order scheme, however, is computationally more efficient. © 2002 Published by Elsevier Science Ltd.

Keywords: Large-eddy simulation; Upwind-based scheme; Compact scheme; Subgrid scale model

1. Introduction

Increasing experience of how to apply large-eddy simulation (LES) and the steady improvement in computer performance has meant that more and more flows of industrial interest are coming within range of analysis by LES. Almost all approaches use body-fitted grids to resolve the computational domain and most of the numerical methods are based on finite-difference or finite-volume schemes. Since the formulation of formally second-order schemes on curvilinear meshes is

---

* Corresponding author.
E-mail address: office@aia.rwth-aachen.de (M. Meinke).

relatively straightforward, such schemes are very popular. To obtain accurate turbulence statistics, however, second-order accurate methods need a relatively high grid resolution. This drawback can be overcome when spectral methods are used. Due to their high accuracy, reliable solutions can be computed using comparatively coarse meshes. In curvilinear formulations, however, the computational costs of these schemes are large and non-periodic boundary conditions, that always occur in complex flow fields, require a special treatment, i.e., the Fourier functions have to be replaced by other orthogonal functions. Another idea is to use high-order upwind schemes. They are well established on arbitrary grids, but they suffer from a dissipative truncation error, which interferes with the subgrid scale model [2]. The truncation error of such schemes can become so dominant that the highest wave numbers are damped primarily by this dissipative error and less by the subgrid scale model. With centrally formulated schemes the dissipative error vanishes, but at the same time such schemes are more difficult to apply for non-trivial geometries, because numerical instabilities may occur due to stretched or non-orthogonal grids.

Hence, there is a need to investigate the numerical behavior of high-order central-difference schemes on grids with an arbitrary grid-point spacing. We base our high-order method on the compact finite-difference formulations by Lele [22] that have a spectral-like resolution ability, but a simpler structure than spectral methods. In simple geometries these methods have already been successfully applied to perform direct numerical simulations, see e.g. Ref. [21]. Unlike former studies, we do not use analytic transformations to locally refine the grid, since flows past or through complex geometries require body-fitted grids that cannot be generated analytically. Therefore, the compact scheme is formulated in a general frame of reference and the metric terms are computed using the same difference approximations. In the interior of the computational domain our scheme is sixth-order accurate, while approaching the physical boundaries the accuracy is reduced to fourth- and then third-order. To reduce the phenomenon of aliasing, i.e., the misinterpretation of short-wave-length components as long-wave-length components, the inviscid terms of the Navier–Stokes equations are discretized in their skew-symmetric form. Aside from the compact scheme we use an advective upstream splitting method (AUSM)-based second-order accurate method for the same flow problems to assess the quality of the high-order solutions. To reduce the numerical dissipation of the scheme, the pressure splitting in the AUSM method is reformulated to a central approximation. Other upwind schemes including a flux-difference formulation of second-order accuracy and an essentially non-oscillatory (ENO) approach of third- and fourth-order accuracy were also tested. In numerous test simulations of the channel flow, however, all turbulent fluctuations were damped by the truncation error of these schemes and a laminar flow field occurred. For this reason, we consider in this study only findings of compact and AUSM schemes.

The purpose of the paper is twofold. First, we deal with the issue whether the larger computational effort of a high-order compact scheme is compensated by the fewer number of grid points to achieve the same accuracy compared to a second-order scheme in LES on non-equidistant curvilinear meshes, such that a more efficient method results. Second, the importance of the contribution of the truncation error and various subgrid scale models to the solution is addressed. In Ref. [17] it is stated that a discretization scheme of higher than second-order accuracy is required, since otherwise the truncation error will be of the same order of magnitude as the contribution of a subgrid model. Considering LES on curvilinear meshes, will a sixth-order scheme be accurate enough such that subgrid modeling will make a difference in the solution?

The paper is organized as follows. After the presentation of the filtered Navier–Stokes equations and the subgrid scale models we briefly describe the AUSM scheme and in more detail the compact finite-difference scheme. The first part of the results consists of numerical simulations of the laminar flow past a cylinder and the turbulent channel flow. Both flows are computed for validation purposes. Subsequently, to compare the various methods of solutions, the plane turbulent jet is investigated.

2. Governing equations

Let ϱ denote the density, u_β ($\beta = 1, 2, 3$) the Cartesian velocity components in the x_β-directions, and E, p the total specific internal energy and the static pressure. Then, neglecting body forces and heat sources, the conservative, non-dimensional form of the Navier–Stokes equations for the time-dependent, three-dimensional flow of a compressible fluid can be written in a generalized frame of reference $\xi_\alpha = \xi_\alpha(x_\beta)$ ($\beta = 1, 2, 3$) ($\alpha = 1, 2, 3$)

$$J\frac{\partial Q}{\partial t} + \frac{\partial H_\alpha}{\partial \xi_\alpha} = 0,$$

where the quantity $Q = [\varrho, \varrho u_\beta, \varrho E]^{\mathrm{T}}$ represents the vector of the conservative variables, $J = |\partial(\xi_\alpha)/\partial(x_\beta)|$ is the metric Jacobian, and the quantity H_α denotes the difference of the inviscid fluxes F_α^{I} and the viscous fluxes F_α^{V}

$$H_\alpha = F_\alpha^{\mathrm{I}} - F_\alpha^{\mathrm{V}} = J\begin{pmatrix} \varrho U_\alpha \\ \varrho u_\beta U_\alpha + p\partial\xi_\alpha/\partial x_\beta \\ U_\alpha(\varrho E + p) \end{pmatrix} + \frac{J}{Re}\begin{pmatrix} 0 \\ \sigma_{\beta\varphi}\partial\xi_\alpha/\partial x_\varphi \\ (u_\beta\sigma_{\beta\varphi} + q_\varphi)\partial\xi_\alpha/\partial x_\varphi \end{pmatrix}.$$

Using Stokes' hypothesis the stress tensor $\sigma_{\alpha\beta}$ reads

$$\sigma_{\alpha\beta} = -2\mu(S_{\alpha\beta} - \tfrac{1}{3}S_{\varphi\varphi}\delta_{\alpha\beta}) \qquad \text{with} \qquad S_{\alpha\beta} = \tfrac{1}{2}\left(\frac{\partial u_\alpha}{\partial\xi_\varphi}\frac{\partial\xi_\varphi}{\partial x_\alpha} + \frac{\partial u_\beta}{\partial\xi_\varphi}\frac{\partial\xi_\varphi}{\partial x_\beta}\right).$$

The quantities U_α and q_α represent the contravariant velocity $U_\alpha = u_\beta\partial\xi_\alpha/\partial x_\beta$ and Fourier's heat flux

$$q_\alpha = -\frac{k}{Pr(\gamma - 1)}\frac{\partial T}{\partial x_\alpha},$$

where T is the temperature and γ the ratio of specific heats. The Reynolds and the Prandtl number are denoted by $Re = \varrho_\infty u_\infty L/\mu_\infty$ and $Pr = \mu_\infty c_p/k_\infty$. The molecular viscosity is evaluated using $\mu = T^{0.72}$. Assuming a constant Prandtl number the relation $k(T) = \mu(T)$ holds for the thermal conductivity.

When central discretizations are used to approximate the conservation equations, the phenomenon of aliasing occurs. It is well-known that in incompressible flows this kind of error can be reduced by rewriting the fundamental equations in the skew-symmetric form. Although the theory does not fully apply to compressible fluids, computations show a certain dealiasing effect also for compressible flows [32]. Following [4] the skew-symmetric form in body-fitted coordinates, that ensures the conservation of the turbulence energy, reads

$$J\frac{\partial Q}{\partial t} + F_{\alpha,s}^{\mathrm{I}} = \frac{\partial F_{\alpha}^{\mathrm{V}}}{\partial \xi_\alpha}$$

with

$$F_{\alpha,s}^{\mathrm{I}} = \frac{1}{2}\begin{pmatrix} 2\frac{\partial(J\varrho U_\alpha)}{\partial\xi_\alpha} \\ \frac{\partial}{\partial\xi_\alpha}(J\varrho u_\beta U_\alpha) + J\varrho U_\alpha\frac{\partial u_\beta}{\partial\xi_\alpha} + u_\beta\frac{\partial(J\varrho U_\alpha)}{\partial\xi_\alpha} \\ \frac{\partial}{\partial\xi_\alpha}(J\varrho U_\alpha H) + J\varrho U_\alpha\frac{\partial H}{\partial\xi_\alpha} + H\frac{\partial J\varrho U_\alpha}{\partial\xi_\alpha} \end{pmatrix} + \begin{pmatrix} 0 \\ \frac{\partial}{\partial\xi_\alpha}(Jp\frac{\partial\xi_\alpha}{\partial x_\beta}) \\ 0 \end{pmatrix},$$

where $H = E + p/\varrho$ is the total enthalpy.

If we seek a solution via a direct numerical simulation, the Navier–Stokes equations are discretized in the aforementioned formulation. In case of a LES, however, a spatial filter is applied to yield the resolvable-scale equations. A filter operation separates the large-scale part $\overline{\Phi}(\vec{x},t)$

$$\overline{\Phi}(\vec{x},t) = \int_\Omega G(\vec{x},\vec{y},\varDelta(\vec{x}))\Phi(\vec{y},t)\,\mathrm{d}\vec{y},$$

from the fine-scale part $\Phi'(\vec{x},t)$ such that

$$\Phi(\vec{x},t) = \overline{\Phi}(\vec{x},t) + \Phi'(\vec{x},t).$$

The quantity Ω represents the flow domain, $\varDelta$ denotes the filter width that defines the length scale associated with the spatial filter, and G is the filter kernel, which is a localized function. Introducing Favre's [14] density-weighted filter operation $\widetilde{\Phi} = \overline{\varrho\Phi}/\overline{\varrho}$ for the Cartesian velocity components, the temperature, and the energy we obtain the filtered conservation equations

$$J\frac{\partial\widetilde{Q}}{\partial t} + \frac{\partial\widetilde{H}_\alpha}{\partial\xi_\alpha} = 0$$

with $\widetilde{Q} = (\overline{\varrho}, \overline{\varrho}\tilde{u}_\beta, \overline{\varrho}\widetilde{E})^{\mathrm{T}}$ and

$$\widetilde{H}_\alpha = \widetilde{F}_\alpha^{\mathrm{I}} - \widetilde{F}_\alpha^{\mathrm{V}} = J\begin{pmatrix} \overline{\varrho}\widetilde{U}_\alpha \\ \overline{\varrho}\tilde{u}_\beta\widetilde{U}_\alpha + \overline{p}\partial\xi_\alpha/\partial x_\beta \\ \widetilde{U}_\alpha\overline{\varrho}\widetilde{E} + \overline{U_\alpha p} \end{pmatrix} + \frac{J}{Re}\begin{pmatrix} 0 \\ \frac{\partial\xi_\alpha}{\partial x_\varphi}(\tilde{\sigma}_{\beta\varphi} + \tilde{\tau}_{\beta\varphi}) \\ \frac{\partial\xi_\alpha}{\partial x_\varphi}(\widetilde{\Theta}_\varphi + \widetilde{\Gamma}_\varphi) \end{pmatrix},$$

where $\overline{p}$ is determined by the filtered equation of state

$$\overline{p} = \frac{1}{\gamma}\overline{\varrho}\widetilde{T}.$$

The convective terms generate the stress tensor of the sub-grid scale structures, which can be written as follows, if the spatial filter operator obeys the Reynolds averaging rules

$$\tilde{\tau}_{\alpha\beta} = \overline{\varrho}\left(\widetilde{U_\alpha u_\beta} - \widetilde{U}_\alpha\tilde{u}_\beta\right) = \overline{\varrho}\widetilde{U}'_\alpha\tilde{u}'_\beta.$$

The Stokes tensor $\tilde{\sigma}_{\alpha\beta} = -2\mu\left(\widetilde{S}_{\alpha\beta} - \frac{1}{3}\widetilde{S}_{\varphi\varphi}\delta_{\alpha\beta}\right)$ can be expressed via the filtered quantities

$$\widetilde{S}_{\alpha\beta} = \frac{1}{2}\left(\frac{\partial\tilde{u}_\alpha}{\partial\xi_\varphi}\frac{\partial\xi_\varphi}{\partial x_\beta} + \frac{\partial\tilde{u}_\beta}{\partial\xi_\varphi}\frac{\partial\xi_\varphi}{\partial x_\alpha}\right),$$

and the energy equation contains the expressions

$$\widetilde{\Theta}_\alpha = \overline{u_\beta \sigma_{\alpha\beta}} + \tilde{q}_\alpha,$$

$$\widetilde{\Gamma}_\alpha = \overline{\varrho}(\widetilde{Eu_\alpha} - \widetilde{E}\tilde{u}_\alpha).$$

The terms $\overline{U_\alpha p}$ and $\overline{u_\beta \sigma_{\alpha\beta}}$, the fine-scale stresses $\tilde{\tau}_{\alpha\beta}$ and the energy flux $\widetilde{\Gamma}_\alpha$ are unknown. Following Moin et al. [25] and Erlebacher et al. [13] direct numerical simulations indicate that the products can be approximated by

$$\overline{U_\alpha p} = \widetilde{U}_\alpha \overline{p},$$

$$\overline{u_\beta \sigma_{\alpha\beta}} = \tilde{u}_\beta \tilde{\sigma}_{\alpha\beta}.$$

This leaves the subgrid terms $\tilde{\tau}_{\alpha\beta}$ and $\widetilde{\Gamma}_\alpha$ the only expressions that have to be modeled. We apply two subgrid scale models both of which comprise the eddy viscosity ansatz. The anisotropic part of the subgrid scale stress $\tilde{\tau}_{\alpha\beta}^A$ is modeled by

$$\tilde{\tau}_{\alpha\beta}^A = \overline{\varrho}(\widetilde{U}'_\alpha \tilde{u}'_\beta - \tfrac{1}{3}\widetilde{U}'_\varphi \tilde{u}'_\varphi \delta_{\alpha\beta}) = -2\overline{\varrho}\nu_t(\widetilde{S}_{\alpha\beta} - \tfrac{1}{3}\widetilde{S}_{\varphi\varphi}\delta_{\alpha\beta}) = \overline{\varrho}\frac{\nu_t}{\mu}\tilde{\sigma}_{\alpha\beta},$$

where ν_t is the eddy viscosity of the fine scales. The isotropic part $\tilde{\tau}_{\alpha\beta}^I = (1/3)\widetilde{U}'_\varphi \tilde{u}'_\varphi \delta_{\alpha\beta}$ has been shown by Erlebacher et al. [13] to be negligible for moderate Mach numbers and is also neglected here.

The most widely used subgrid scale model is the Smagorinsky model [30] that is based on the gradient transport hypothesis and a dimension argument. The subgrid scale eddy viscosity is given by

$$\nu_t = C_S^2 \Delta^2 |\widetilde{S}|$$

in which $|\widetilde{S}|$ represents the absolute value of the strain-rate tensor $|\widetilde{S}| = (2\widetilde{S}_{\alpha\beta}\widetilde{S}_{\alpha\beta})^{1/2}$ and C_S is the Smagorinsky constant which is set to $C_S = 0.1$. In regions close to a rigid wall the van Driest damping function is used to get the correct near wall behavior

$$C_{S\ wall} = C_S(1 - \exp(-y^+/25))^2,$$

where y^+ is the distance from the wall in viscous wall units.

The Smagorinsky model predicts always a positive eddy viscosity, even in laminar flow. Although this property makes this model not suited for transitional flows, its dissipative character stabilizes numerical solutions based on central schemes. Unfortunately, the gradient transport hypothesis is not adequate so that results with this model are in a poor correlation with the true turbulent stress. In addition, C_S is not a universal constant, so that it has to be adapted to different flow conditions. To overcome some of the disadvantages of the Smagorinsky model Germano introduced a dynamic procedure, based on the application of the Smagorinsky model at two different filter levels, to determine the Smagorinsky constant [16]. Additionally to the filter width Δ, a test filter width $\overline{\Delta} > \Delta$ is used. Applying the test filter to the filtered equations the twice filtered stresses are obtained

$$\hat{\tau}_{\alpha\beta} = \overline{\overline{\varrho \widetilde{U_\alpha u_\beta}}} - (\overline{\overline{\varrho}\widetilde{U}_\alpha \overline{\varrho}\overline{\tilde{u}}_\beta})\overline{\overline{\varrho}}.$$

The stress tensor $\tilde{\tau}_{\alpha\beta}$ is also test filtered

$$\overline{\tilde{\tau}}_{\alpha\beta} = \overline{\widetilde{\varrho U_\alpha u_\beta}} - \overline{\varrho \widetilde{U}_\alpha \tilde{u}_\beta},$$

such that the difference $\hat{\tau}_{\alpha\beta} - \overline{\tilde{\tau}}_{\alpha\beta}$ yields

$$\hat{\tau}_{\alpha\beta} - \overline{\tilde{\tau}}_{\alpha\beta} = \overline{\overline{\varrho}\widetilde{U}_\alpha \tilde{u}_\beta} - (\overline{\varrho \widetilde{U}_\alpha} \overline{\varrho \tilde{u}_\beta})/\overline{\overline{\varrho}} = L_{\alpha\beta},$$

which is called the Germano identity. The Leonard terms $L_{\alpha\beta}$ on the right-hand side can be computed explicitly. The Germano identity, that is postulated to hold for the modeled fine-scale stresses,

$$\tilde{\tau}^m_{\alpha\beta} = -2(C_S \varDelta)^2 \overline{\varrho}|\widetilde{S}|\left(\widetilde{S}_{\alpha\beta} - \tfrac{1}{3}\widetilde{S}_{\varphi\varphi}\delta_{\alpha\beta}\right) = -2(C_S \varDelta)^2 A_{\alpha\beta},$$

$$\hat{\tau}^m_{\alpha\beta} = -2\left(C_S \overline{\varDelta}\right)^2 \overline{\overline{\varrho}}|\overline{\widetilde{S}}|\left(\overline{\widetilde{S}}_{\alpha\beta} - \tfrac{1}{3}\overline{\widetilde{S}}_{\varphi\varphi}\delta_{\alpha\beta}\right) = -2\left(C_S \overline{\varDelta}\right)^2 B_{\alpha\beta},$$

is applied to the anisotropic part of the Leonard terms

$$\mathrm{L}^A_{\alpha\beta} = \overline{\overline{\varrho}\widetilde{U}_\alpha \tilde{u}_\beta} - \left(\overline{\varrho \widetilde{U}_\alpha}\,\overline{\varrho \tilde{u}_\beta}\right)/\overline{\overline{\varrho}} - \tfrac{1}{3}\left(\overline{\overline{\varrho}\tilde{u}_\varphi \tilde{u}_\varphi} - \left(\overline{\varrho \tilde{u}_\varphi}\,\overline{\varrho u_\varphi}\right)/\overline{\overline{\varrho}}\right)\delta_{\alpha\beta} = \hat{\tau}^m_{\alpha\beta} - \overline{\tilde{\tau}}^m_{\alpha\beta}.$$

Since this expression for the Smagorinsky constant is a system of equations for the single unknown C_S, a least square approach is used to calculate the coefficient [23]

$$(C_S \varDelta)^2 = -\frac{1}{2}\frac{\langle \mathrm{L}^A_{\alpha\beta} N_{\alpha\beta}\rangle}{\langle N_{\varphi\delta} N_{\varphi\delta}\rangle},$$

with $N_{\alpha\beta} = \left(\frac{\overline{\varDelta}}{\varDelta}\right)^2 B_{\alpha\beta} - \overline{A}_{\alpha\beta}$. The brackets $\langle\cdot\rangle$ denote an average over the homogeneous directions that is introduced to avoid zero-divide. The quantity C_S is dynamically computed using the foregoing procedure. In regions where small-scale structures are not significant, C_S becomes small such that no wall damping functions are required when the dynamic model is used.

To model the fine-scale energy flux $\widetilde{\varGamma}_\alpha$ we adopt the same approximation as for the stress tensor $\tilde{\tau}_{\alpha\beta}$ [10]. Based on a gradient–flux ansatz $\widetilde{\varGamma}_\alpha$ is formulated as a function of the eddy viscosity v_t

$$\widetilde{\varGamma}_\alpha = -\frac{\overline{\varrho}}{\gamma_0 - 1}\frac{v_t}{Pr_t}\frac{\partial \widetilde{T}}{\partial x_\alpha},$$

where the turbulent Prandtl number Pr_t is set 0.5 [12].

3. Numerical method

First, we introduce the algorithm to numerically integrate the approximated Navier–Stokes equations in time, and then, we present two discretization schemes for the spatial derivatives.

3.1. Time integration

In LES the maximum possible time step is primarily determined by the time scales of the turbulent fluctuations, less by the stability constraint of the numerical scheme. For example, using

an implicit method Choi and Moth [7] encounter a laminarization if the time step is essentially larger than that given by the stability limit of an appropriate explicit method. Therefore, we apply an explicit five-step Runge–Kutta method [19] to propagate the vector of solution $\widetilde{Q}$ from time level n to $n+1$

$$
\begin{aligned}
\widetilde{Q}^0 &= \widetilde{Q}^n \\
&\vdots \\
\widetilde{Q}^l &= \widetilde{Q}^0 - \alpha_l \Delta t R(\widetilde{Q}^{l-1}) \\
&\vdots \\
\widetilde{Q}^{n+1} &= \widetilde{Q}^5,
\end{aligned}
$$

where l, n denote the step index $l = 1, \ldots, 5$, and the time level, $\Delta t = t^{n+1} - t^n$ is the time step, and R represents the flux integral over a cell volume defined by the computational grid. Using the Runge–Kutta coefficients $\alpha_l = (1/4, 1/6, 3/8, 1/2, 1)$ a method of second-order accuracy in time with a maximum Courant number of 4 for central schemes results. For comparison a classical Runge–Kutta scheme of fourth-order accuracy was used in combination with the compact scheme. Since the time step had to chosen rather small for stability reasons, the difference in the results was so small that the computationally more efficient scheme of second-order accuracy was used for the most of the simulations presented.

3.2. Spatial discretization

The properties and spatial accuracy of the numerical scheme are determined by the formulation of the inviscid and viscous fluxes at the cell faces. Since the discretization of the nonlinear inviscid terms plays a much more important role in turbulent flows than that of the friction and heat conduction expressions, the viscous terms are approximated, unless otherwise mentioned, by second-order accurate central differences in which the second derivatives are obtained by differences of the fluxes through the cell faces, which contain first derivative terms.

Results from direct numerical simulations show that the subgrid scale stresses are of the order $\mathcal{O}(h^2)$. Therefore, a large-eddy simulation has to be conducted with a scheme of at least second-order accuracy. Additionally, the numerical dissipation of the approximation has to be as low as possible, since the small scales of the turbulent flows are significantly affected by the numerical dissipation. Due to the inherent interaction between the various scales a falsification of the representation of all turbulent structures results [29].

For this reason, central difference schemes are very popular in LESs of incompressible flows. Unfortunately, the standard central differences approximations tend to be unstable in compressible flows, unless some kind of artificial numerical dissipation is added. To circumvent these difficulties we use for the discretization of the inviscid fluxes a mixed central-upwind AUSM-scheme that is based on the method of Liou and Steffen [24]. Moreover, high-order compact finite-difference methods, also called Padé methods, are introduced to analyze the dependence of the impact of the subgrid scale model and of the efficiency of the algorithm on the accuracy of the approximation of the inviscid fluxes on curvilinear grids. In the following the AUSM and the compact methods are briefly described.

3.2.1. AUSM method

The AUSM method was introduced by Liou and Steffen [24] who split the inviscid fluxes into a convective and a pressure term and reformulated the convective expression by inserting the local sound velocity c. Dropping the tildes and the overbars this leads to

$$F_\alpha^I = F_\alpha^c + F_\alpha^p = \frac{U_\alpha}{c} \underbrace{\begin{pmatrix} \varrho c \\ \varrho c u_\beta \\ \varrho c(E + p/\rho) \end{pmatrix}}_{f_\alpha^c} + \begin{pmatrix} 0 \\ p\partial\xi_\alpha/\partial x_\beta \\ 0 \end{pmatrix}.$$

The numerical flux F_α^c on the cell face, e.g. $i \pm \frac{1}{2}$, j, k, reads

$$F_\alpha^c = \frac{1}{2}\left[\frac{Ma_\alpha^+ + Ma_\alpha^-}{2}\left(f_\alpha^{c+} + f_\alpha^{c-}\right) + \frac{|Ma_\alpha^+ + Ma_\alpha^-|}{2}\left(f_\alpha^{c+} - f_\alpha^{c-}\right)\right]_{i\pm\frac{1}{2},j,k},$$

where the fluxes $f_\alpha^{c\pm}$ and the Mach numbers $Ma_\alpha^\pm$ are determined by left and right interpolated variables obtained using a monotonic upstream centered schemes for conservation laws (MUSCL) approach for the primitive variables [34].

To compute the remaining pressure term various pressure-splitting formulations are given in the literature [7] that can be written in a general form

$$p^\pm = p^\pm\left(\tfrac{1}{2} \pm \chi Ma_\alpha^\pm\right).$$

The parameter χ, that represents the rate of change of the pressure ratio with respect to the local Mach number, defines what kind of pressure splitting is used and as such determines the numerical dissipation of the scheme. For $\chi = 0.5$ a pure upwind pressure splitting with such a large numerical dissipation results that in LESs of channel flow an unphysical laminarization was observed [3]. A central splitting with clearly less numerical dissipation is obtained at $\chi = 0$. If, however, strongly stretched meshes are used, pressure oscillations may occur that could lead to an unstable solution. This problem can be remedied by inserting somewhat more upwinding in the scheme which is achieved by letting the parameter χ be in the range $0 \leqslant \chi \leqslant 1/96$. Since we use smooth curvilinear stretched grids the dissipation parameter χ can be set $\chi = 0$ in all the computations discussed in this study.

3.2.2. Compact finite-difference schemes

We turn now to the discussion of the compact finite-difference schemes. These schemes, that were already introduced by Collatz in Ref. [8], are analyzed in great detail in Ref. [22] and extended in Ref. [36]. To improve the accuracy compared to standard finite-difference formulations, compact finite-difference schemes copy the global dependence of spectral methods by coupling first derivative terms over all mesh points. This is achieved by approximating a set of derivatives, i.e., more than one term, by finite-difference expressions. Reducing the formulation in Ref. [22] to the tridiagonal one-parameter (α) family the central compact finite-difference schemes read

$$\alpha f_{i+1}' + f_i' + \alpha f_{i-1}' = b\frac{f_{i+2} - f_{i-2}}{4h} + a\frac{f_{i+1} - f_{i-1}}{2h}, \tag{1}$$

where the coefficients a, b, and α determine the spectral resolution and the formal truncation error of the approximation.

Near non-periodic boundaries approximations for the derivatives need to be non-central, i.e., one-sided. Maintaining the tridiagonal structure of the inner scheme a general boundary formulation for the first derivative at $i = 1$ can be written as

$$f_1' + \alpha f_2' = \frac{1}{h}(af_1 + bf_2 + cf_3). \tag{2}$$

As in the case of the interior scheme the values of the coefficients define the numerical properties of the approximation. Based on the findings of a Fourier analysis for the dispersive and dissipative errors of the various compact finite-difference schemes the following interior and boundary schemes, the coefficients of which are given in Table 1, with the best overall spectral properties are chosen to discretize the Navier–Stokes equations [28]. The method is denoted Padé-3/4/6 since the formal spatial order of accuracy changes from $\mathcal{O}(h^3)$ at the first inner point via $\mathcal{O}(h^4)$ at the second inner point to $\mathcal{O}(h^6)$ in the interior of the computational domain. To ensure a discrete analogy to the conservation constraint between the various schemes defined by the different coefficients for the near boundary mesh points, weights at the four nodes adjacent to the boundary are introduced according to Lele. These weights are uniquely determined when the schemes, i.e., the coefficients to be used in the interior, and at $i = 3$ and $i = \text{Imax-2}$ are specified [22]. For this reason, the coefficients at $i = 3$ and $i = \text{Imax-2}$ are also given in Table 1.

Since the central compact finite-difference schemes do not possess any numerical damping, high frequency oscillations, that are generated near boundaries due to the reduction of the order of accuracy in these regions and due to the approximate formulation of boundary conditions, are removed by an explicit low-pass filtering in physical space with a formal truncation error of fourth-order. Using the spatial step size as filter width, a one-parameter family of filtering schemes reads [22]

$$\psi \overline{Q}_{i+1} + \overline{Q}_i + \psi \overline{Q}_{i-1} = \frac{5 + 6\psi}{8} Q_i + \frac{1 + 2\psi}{4}(Q_{i+1} + Q_{i-1}) + \frac{2\psi - 1}{8}(Q_{i+2} + Q_{i-2}),$$

that has the same tridiagonal structure as the Padé-3/4/6 method. The analysis of the transfer function $T(\omega; \psi)$

$$T(\omega; \psi) = \frac{1}{1 + 2\psi \cos(\omega)}\left[\frac{5 + 6\psi}{8} + \frac{1 + 2\psi}{2}\cos(\omega) + \frac{2\psi - 1}{8}\cos(2\omega)\right],$$

that states what modes are unfiltered at what percentage, shows that for $\psi \to 0.5$ only the highest scaled wave number $\omega = \pi$ is filtered (Fig. 1). At lower values $\psi < 0.5$ a continuous filtering is obtained, i.e., there is no sharp separation between resolved and filtered scales. In this study,

Table 1
Coefficients of the Padé-3/4/6 scheme

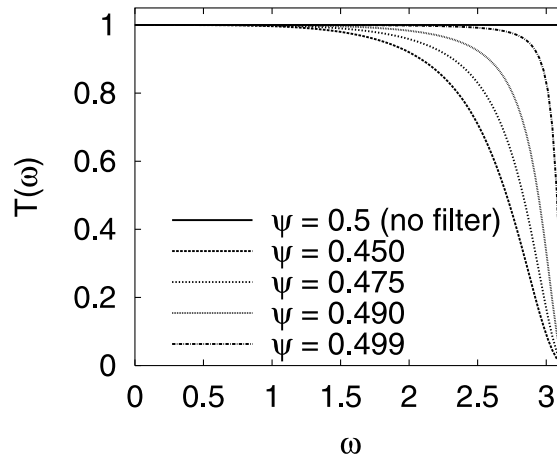| Location	Equation	Coefficients				Order of truncation error
		α	a	b	c	
$i = 1$, $i = \text{Imax}$	2	2	−5/2	2	1/2	3
$i = 2$, $i = \text{Imax-1}$	1	1/4	3/2	0	0	4
$i = 3$, $i = \text{Imax-2}$	1	37/112	87/56	3/28	0	6
$4 \leqslant i \leqslant \text{Imax-3}$	1	1/3	14/9	1/9	0	6

Fig. 1. Transfer function $T(\omega)$ vs. the scaled wave number ω for various values of the filter parameter ψ.

unless otherwise mentioned, the chosen ψ-value is in the range $0.49 \leqslant \psi \leqslant 0.5$. At non-periodic boundaries the filtering schemes

$$\overline{Q}_1 = \frac{15}{16}Q_1 + \frac{1}{16}(4Q_2 - 6Q_3 + 4Q_4 - Q_5),$$

$$\overline{Q}_2 = \frac{3}{4}Q_2 + \frac{1}{16}(4Q_1 + 6Q_3 - 4Q_4 + Q_5),$$

that are also fourth-order accurate, are used.

As already mentioned above, central compact finite-difference schemes are susceptible to aliasing. The Padé-3/4/6 method is therefore applied to the skew-symmetric form of the governing equations since this special formulation of the convective terms minimizes aliasing even in compressible flows [32]. Furthermore, an explicit filtering scheme is used to remove high frequency components in the solution. This filtering is applied every fifth time step. Due to the upwind-based formulation in the AUSM scheme for the derivatives of the convective terms, it does not suffer from aliasing such that the standard conservative form of the Navier–Stokes equations is approximated using the AUSM method.

4. Results

In the following results of several external and internal flow problems are presented. First, the flow past a circular cylinder at a diameter based Reynolds number of $Re_\infty = 100$ is simulated, mainly to validate the Padé-3/4/6 scheme. Moreover, we will discuss the susceptibility of the solution of the compact scheme to the filtering and to various approximations of the viscous terms. Next, we study turbulent channel flows for two reasons. On the one hand, we will show the quality of the results of the AUSM scheme and as such it will be established as a reference method. On the other hand, we will use the channel flow distributions as inflow data for the turbulent jet. In the case of the jet flow we will juxtapose the solutions of the AUSM and the

Padé-3/4/6 method to investigate the impact of the order of approximation of the inviscid terms on the effects of the subgrid scale model on the findings and on the efficiency of the algorithm.

4.1. Flow past a cylinder

To validate the Padé-3/4/6 scheme a numerical study of the laminar flow around a circular cylinder is performed. This investigation is also used to show the dependence of the results of the compact scheme on different values of the filter parameter ψ and on various discretizations of the viscous expressions. At a Reynolds number of $Re_\infty = 100$ and a Mach number of $M_\infty = 0.3$ a vortex street develops with a Strouhal number Sr in the range of $0.157 \leqslant Sr \leqslant 0.167$ [15]. A fine and a coarse O-type mesh is used with 257×129 and 129×65 azimuthally and radially distributed grid points on a computational domain whose far field boundary is located 10 diameters off the cylinder. The inflow and outflow boundary conditions are determined by the characteristics of the one-dimensional Euler-equations. The no-slip and adiabatic condition are imposed on solid walls. To initialize the computation an undisturbed flow field is assumed.

Besides the aforementioned AUSM and Padé-3/4/6 methods, a pure Padé scheme using compact finite-differences for the inviscid and viscous terms is applied to show the impact of a high-order approximation of the viscous part on the solution. Although the differences between the various methods are rather small the results in Table 2 provide evidence that the pure Padé method is more sensitive to grid coarsening than the AUSM method, e.g. the differences in the Strouhal number and the minimum drag coefficient are $3 \times 10^{-4}/6 \times 10^{-4}$ and $0.0137/0.0213$ for the AUSM/Padé method, respectively, and that changing the value of the filter parameter ψ has a stronger impact on the solution than switching the discretization of the viscous terms from a sixth-order to a second-order approximation. It should be noted that the Padé scheme for the viscous terms is much more costly in terms of computing time. For this reason, the following LESs are performed with the central differences of second-order accuracy for the viscous expressions.

4.2. Turbulent channel flow

The turbulent channel flow serves as a test case to prove the AUSM method an appropriate means to deliver a reference solution for the jet flow problem and to determine the velocity and temperature distribution on the inflow boundary when the turbulent jet is simulated. The

Table 2
Laminar flow past a circular cylinder, $Re_\infty = 100$, $M_\infty = 0.3$, fine grid 257×129 az. × rad., and coarse grid 257×129 az. × rad. grid points. Strouhal number Sr, maximum and minimum drag coefficient $c_{d,max}$, $c_{d,min}$, amplitude of the lift coefficient $\Delta c_l/2 = (c_{l,max} - c_{l,min})/2$, filter parameter ψ

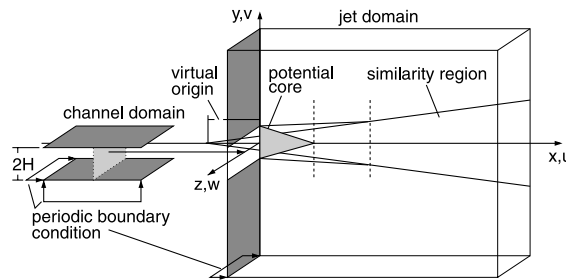| Grid	Inviscid terms	Viscous terms	Filter ψ	Sr	$c_{d,max}$	$c_{d,min}$	$\Delta c_l/2$
Fine	AUSM	Central	–	0.1634	1.3840	1.3673	0.3327
Fine	Padé	Padé	0.495	0.1632	1.3780	1.3664	0.3338
Fine	Padé	Padé	0.475	0.1621	1.3768	1.3581	0.3347
Fine	Padé	Central	0.495	0.1636	1.3841	1.3709	0.3367
Coarse	AUSM	Central	–	0.1631	1.3717	1.3536	0.3294
Coarse	Padé	Padé	0.495	0.1626	1.3655	1.3451	0.3254

Fig. 2. Domain of integration and coordinate system for channel and jet flow simulation.

dynamics of the channel flow field in the proximity of the wall is characterized by coherent structures. Sweeps and ejections form in which high-speed fluid moves toward the wall and vice versa. Between them regions of high and low momentum, so-called high and low speed streaks or streaky structures, develop that are quasi-periodic in the spanwise direction [20]. These slowly moving streaks undergo a characteristic oscillation that ends abruptly and small scale eddies are generated. This well-known phenomenon is called bursting [11]. A direct numerical simulation that shows the intricacy of this flow was introduced in Ref. [20]. This solution and the LES results from Ref. [26] are used as reference solutions in this study.

The coordinate system and a sketch of the geometry of the computational domain is given in Fig. 2. Simulations are carried out for two Reynolds numbers $Re_\tau = 200$ and $Re_\tau = 640a$, where Re_τ is defined $Re_\tau = u_\tau H/v$ using the friction velocity u_τ. These values correspond to Reynolds numbers $Re_{cl} = u_{cl}H/v$ based on the maximum velocity $Re_{cl} = 3800$ and $Re_{cl} = 13\,800$. The Mach number is $Ma = 0.1$ such that compressibility effects can be neglected and the findings can be compared with data of incompressible flows. No-slip and isothermal conditions are specified on the walls and periodic boundary conditions in the spanwise direction. In the streamwise direction the pressure and temperature fluctuations and the mass flow are assumed periodic. Using the relation $Re_\tau = 0.1097Re_{cl}^{0.911}$ [18] the pressure difference $\Delta p = \varrho u_\tau^2 L/H$ that drives the flow is determined by the maximum velocity.

To investigate the dependence of the solution on the mesh resolution, different grids on computational domains with varying dimensions are used. The essential parameters of the meshes, flow problems, and the reference solutions are given in Table 3. The smallest step size normal to

Table 3
Parameters of simulated channel flows. $2H$ is the height of the channel, $Re_\tau = u_\tau H/v$ and $Re_{cl} = u_{cl}H/v$ are the Reynolds numbers based on the friction velocity u_τ and the maximum velocity u_{cl}

Case	Re_τ	Re_{cl}	$(x \times y \times z)/H$	Grid points $x \times y \times z$	Δ_x^+	$\Delta_{y_{min}}^+$	Δ_z^+	Simulation
1	200	3800	$10 \times 2 \times 3$	$99 \times 49 \times 41$	20.4	2.0	15.0	LES
2	200	3800	$10 \times 2 \times 5$	$65 \times 33 \times 33$	31.2	2.0	31.2	LES
3	200	3800	$5 \times 2 \times 3$	$51 \times 49 \times 41$	20.0	2.0	15.0	LES
4	200	3800	$5 \times 2 \times 5$	$33 \times 33 \times 33$	31.2	2.0	31.2	LES
5	640	13 800	$5 \times 2 \times 2$	$129 \times 129 \times 65$	25.0	2.0	20.0	LES
[26]	100	3800	$4\pi \times 2 \times \pi$	$48 \times 65 \times 64$	53.0	0.24	13.0	LES
[20]	180	3300	$4\pi \times 2 \times 2\pi$	$192 \times 129 \times 160$	12.0	0.05	7.0	DNS

the wall $\Delta y^+ = 2$ is much larger than that in Kim's DNS $\Delta y^+ = 0.05$ [20] and in Piomelli's LES $\Delta y^+ = 0.24$ [26]. The total number of grid points is comparable with that in the LES of Piomelli, although he used spectral methods instead of finite-difference schemes for his solutions.

After a fully developed turbulent channel or plane jet flow has been reached the simulations are continued for 500–800 dimensionless time units for the determination of statistical results. Samples of the unsteady solution are stored each 0.1 dimensionless time units so that converged statistical data is obtained for all cases.

Following Taylor [33] we use the turbulence intensity $\sigma(u''_\alpha)$, that is the square root of the variance

$$\sigma^2(u''_\alpha) = \langle u''^2_\alpha \rangle_t,$$

where the notation $\langle g \rangle_t$ represents the time average of g, to define the two-point correlations of the velocity fluctuations

$$R_{u_\alpha u_\beta}(\vec{x}, \vec{r}) = \frac{\langle u''_\alpha(\vec{x}, t) \cdot u''_\beta(\vec{x} + \vec{r}, t) \rangle_t}{\sigma(u''_\alpha(\vec{x})) \cdot \sigma(u''_\beta(\vec{x} + \vec{r}))},$$

which are the basis for the analysis of the turbulent flow fields. The double prime quantities Φ'' are defined as the fluctuating part of the time averaged large scale quantities

$$\Phi'' = \overline{\Phi} - \langle \overline{\Phi} \rangle_t.$$

In Fig. 3 the two-point correlations of the streamwise velocity component in the streamwise and spanwise direction of a fine and coarse grid solution (cases 1,2) are compared with the DNS data from Ref. [20]. No subgrid scale model is used in the LES. The fine-grid LES results are in good agreement with the reference DNS findings whereas a considerable deviation occurs for the coarse grid. The minimum at $z^+ = 55$ corresponds to the half-streak spacing that was also determined by the experiments in Ref. [31]. The vanishing two-point correlations on the fine grid prove the dimensions of the computational domain to be sufficient for case 1. In case 2 the grid resolution is
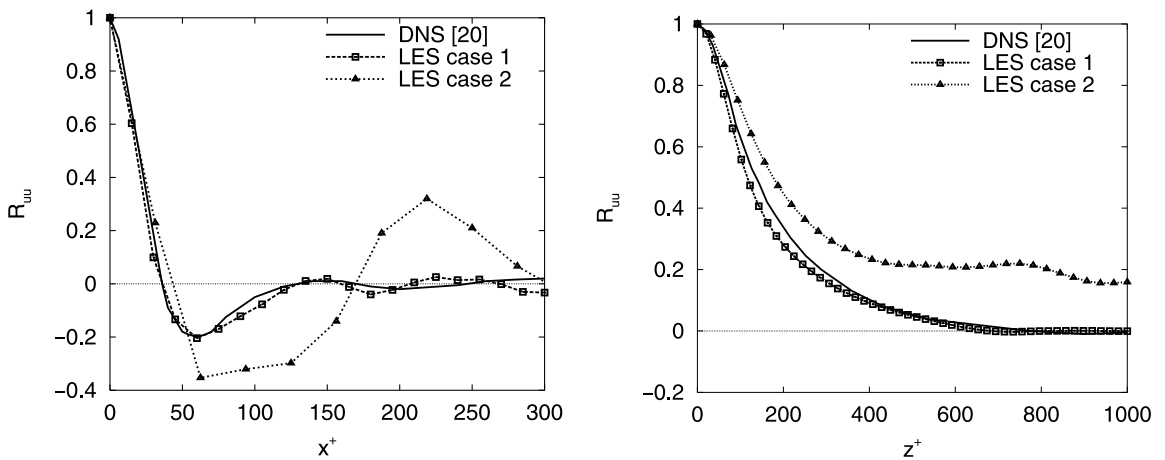

Fig. 3. LES of a turbulent channel flow at a Reynolds number of $Re_\tau = 200$ using the AUSM scheme without subgrid scale model. Two point correlation R_{uu} vs. x^+ and z^+ in comparison with DNS results of Ref. [20] ($Re_\tau = 180$).
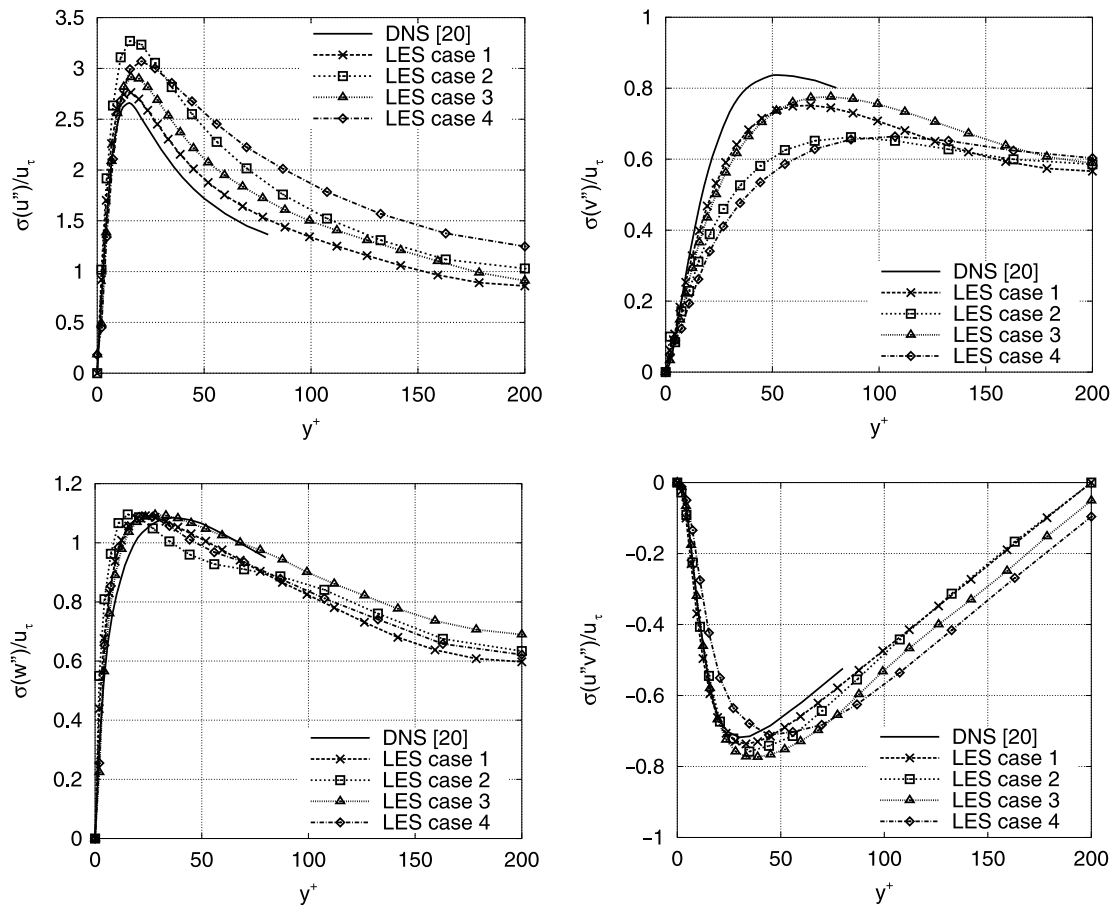
Fig. 4. LES of a turbulent channel flow at a Reynolds number of $Re_\tau = 200$ using the AUSM scheme without subgrid scale model. Comparison of the turbulence intensities and the resolved Reynolds stress component $\sigma(u''v'')/u_\tau$ vs. y^+ with DNS results of Ref. [20] ($Re_\tau = 180$).

too coarse such that the coherent structures cannot be resolved and the two-point correlations do not asymptotically disappear at the boundaries.

The fact that the turbulent energy is only insufficiently redistributed on the coarse mesh can also be seen in the streamwise turbulent intensities in Fig. 4. In comparison with the DNS data they are considerably too large. On the other hand, the turbulent intensities of the fine grid solutions—cases 1 and 3—show the LES results in good agreement with the DNS results of Kim et al. in Ref. [20].

The impact of the subgrid scale model on the LES solution is depicted by means of the turbulent intensities as a function of the normal distance in Fig. 5. The computations are performed on the fine grid of case 1. Both subgrid models, the dynamic and the Smagorinsky model, increase the dissipation which leads to a damping of the small scale structures. Therefore, the redistribution of the energy of the small scales is insufficient and as such the streamwise turbulent intensity is too high, whereas the turbulence intensities of the velocity in the spanwise and wall
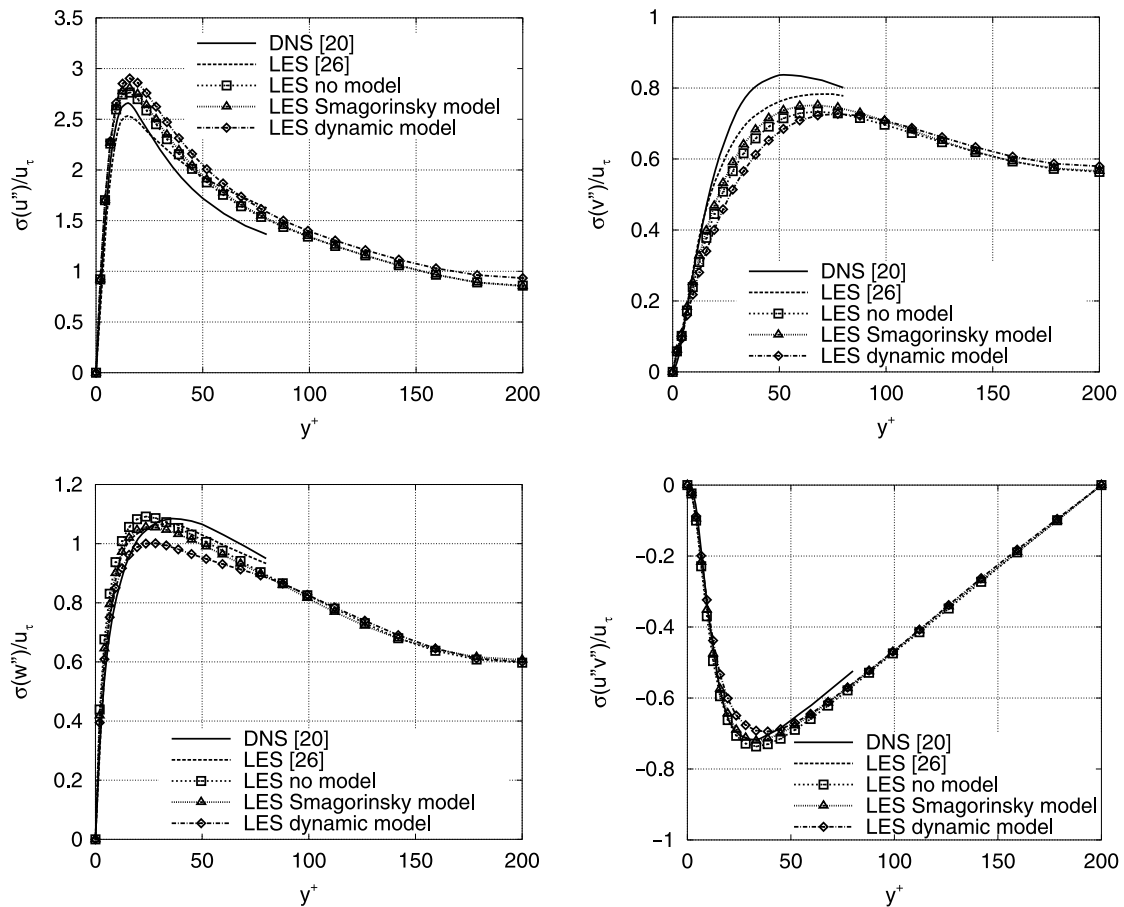
Fig. 5. LES of a turbulent channel flow at a Reynolds number of $Re_\tau = 200$ using the AUSM scheme with different subgrid scale models for case 1. Comparison of the turbulence intensities and the resolved Reynolds stress component $\sigma(u''v'')/u_\tau$ vs. y^+ with DNS results of Ref. [20] ($Re_\tau = 180$) and LES data of Ref. [26].

normal direction are too low. The results agree best with Piomelli's LES and Kim's DNS data when no subgrid model is used. This applies also to the solution of the turbulent channel flow at $Re_\tau = 640$ (Fig. 6) although the differences are much smaller than in the $Re_\tau = 200$ flow problem. That is, even at a higher Reynolds number the application of a subgrid model in a second-order accurate method does not improve the solution defined by the distribution of the statistical variables. This confirms the findings in Ref. [17]. Nevertheless, the agreement with Cabot's LES results for a channel flow [6] at $Re_\tau = 650$ shows the good quality of the present results.

From the findings of the turbulent channel flow it can be concluded that the AUSM scheme without a subgrid model is a reliable method to determine the inflow profile of the LES of a turbulent jet and to compute reference data for such a flow field. For the higher Reynolds number jet, the channel flow of case 5 yields the inflow data, whereas at low Reynolds numbers distributions based on computations of cases 3, 4 are used, since in cases 3, 4 the computational time is only half as large as in cases 1, 2 without any loss in accuracy.
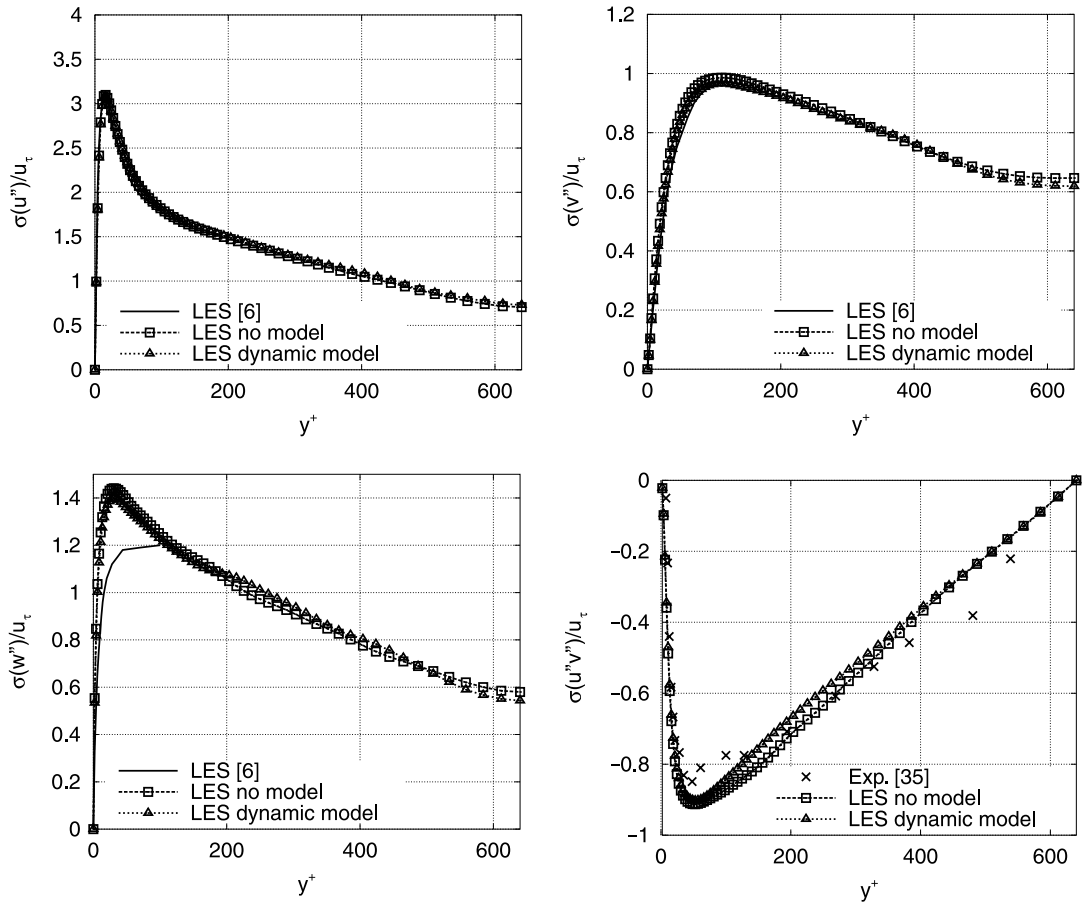
Fig. 6. LES of a turbulent channel flow at a Reynolds number of $Re_\tau = 640$ using the AUSM scheme with different subgrid scale models for case 5. Comparison of the turbulence intensities and the resolved Reynolds stress component $\sigma(u''v'')/u_\tau$ vs. y^+ with LES data of Ref. [6] and experimental data of Ref. [35].

4.3. Turbulent jet

The structure of a plane turbulent jet is shown in Fig. 2. Air is ejected from a plane orifice into air at rest. Shear layers evolve drawing in the surrounding fluid from the sides of the jet. It is not before these shear layers have grown together the velocity on the jet axis is altered. Downstream of this potential core, which is characterized by the constant center-line velocity, a similarity region occurs. In this regime the rate of increase in the half width of the jet $B(x)$ is proportional to x and that of decrease in the center-line velocity is $u_{cl} \sim x^{-1/2}$. The turbulent jet is computed using the AUSM and the Padé-3/4/6 method. Since the comparison of the various numerical methods is the main purpose in this analysis, we prescribe a fully developed turbulent channel flow as inflow profile to avoid any uncertainties that are due to a transitional shear layer. The LESs cover the channel exit, the near field of the jet, and the beginning of the similarity regime. The spreading rate of the jet and the decrease in the velocity at the center of the jet are computed to determine

the quality of the results. Furthermore, an analysis of the turbulence intensities and the Reynolds stresses will be given.

The geometry of the computational domain is shown in Fig. 2. A fully developed turbulent channel flow and the plane turbulent jet are computed simultaneously such that the instantaneous solution in the midplane of the channel flow provides the mass flux and the temperature distribution at the inflow boundary of the jet, whereas the pressure is determined by its instantaneous distribution in the plane immediately downstream from the inflow plane during the computation of the jet. The grid spacing in the streamwise direction is varied using a geometric series. The stretching factor in the normal direction is a function of the x and y coordinates such that a smooth curvilinear mesh is generated. At the far field boundaries in the y-direction the entrainment of the surrounding fluid is approximated by extrapolating the mass flux and the temperature from the interior. The ambient pressure is given by

$$p_\infty = \frac{1}{\gamma}\left(1 + \frac{\gamma - 1}{2}Ma_{\mathrm{cl}}^2\right)^{\frac{\gamma}{1-\gamma}},$$

where Ma_{cl} is the Mach number on the center line of the inflow plane. In the spanwise direction periodic boundary conditions are used and at the far field streamwise boundary non-reflecting boundary conditions are applied [27].

Based on the assumption that the streak spacing is primarily determined by the channel flow the extension of the integration region in the z-direction remains $2.5D$. This means, it is 25 percent larger than that from Dai et al. [9]. The essential data of the computational grids for the turbulent jet flows at two Reynolds numbers $Re_D = 7600$ and $Re_D = 27\,600$ (corresponding to $Re_{\mathrm{cl}} = 3800$ and $Re_{\mathrm{cl}} = 13\,800$ in the channel notation) is summarized in Table 4.

The discussion of the results is organized as follows. We start by presenting a reference solution on the fine grid at $Re_D = 7600$ (case 1) that is computed using the AUSM method without any subgrid model. Next, the influence of the discretization, the subgrid scale model, and the grid resolution is shown by illustrating the distribution of several statistical variables. Finally, the AUSM and Padé based solutions at $Re_D = 27\,600$ are analyzed.

The contours of the averaged and the instantaneous streamwise velocity component in Fig. 7 provide evidence that the computational domain is sufficiently large to ensure that the spreading of the jet does not interact with the far field boundaries in the normal direction. In the immediate vicinity of the slit the turbulent structures are approximately preserved. Further downstream the free-shear layers start to roll up into spanwise vortices. Due to the non-reflecting boundary conditions no perturbations are visible in the velocity distributions near the outflow boundary.

Table 4
Parameters of the simulated jet flows. D is the width of the jet, $Re_D = u_{\mathrm{cl}}D/v = 2Re_{\mathrm{cl}}$ is the Reynolds number based on the width and center-line velocity. Channel case defines the channel flow simultaneously performed to yield the inflow data

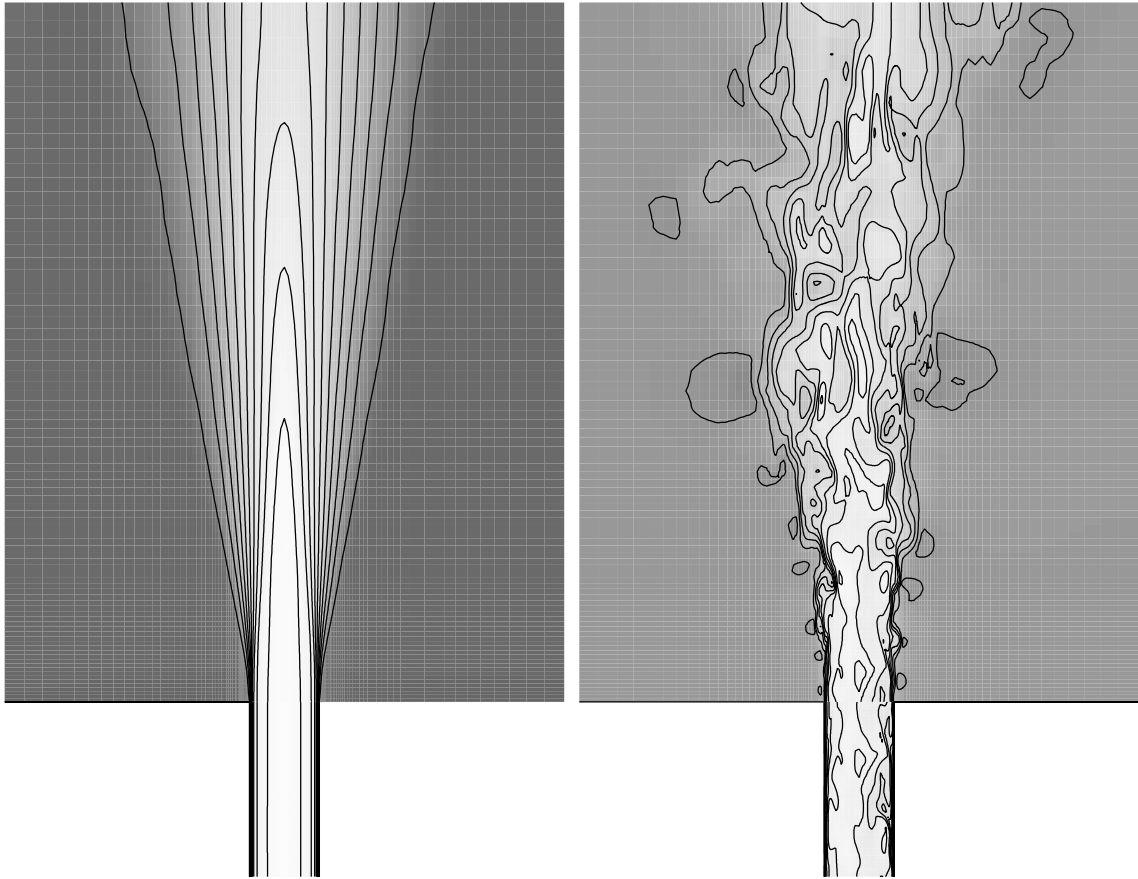| Case	Re_{cl}	Re_D	$(x \times y \times z)/D$	Grid points $x \times y \times z$	Channel case
1	3800	7600	$10 \times 8 \times 2.5$	$81 \times 149 \times 65$	3
2	3800	7600	$12.5 \times 8 \times 2.5$	$65 \times 129 \times 33$	4
3	13\,800	27\,600	$4 \times 8 \times 1$	$81 \times 161 \times 65$	5

Fig. 7. LES (case 1) of a turbulent plane jet flow at $Re_D = 7600$. Time averaged contours of the velocity field (left), contours of the instantaneous velocity field (right).

The decrease of the center-line velocity and the spreading rate of the jet in the streamwise direction asymptotically approaches the similarity solution, i.e., $u_{cl} \sim x^{-1/2}$ that is valid for free turbulent flows and $B \sim x$ holds for $x/D > 6$ [1] (Fig. 8). This is also confirmed by the velocity profiles in different vertical planes in Fig. 9 The distributions are in good agreement with the theoretical data from Ref. [1] and the experimental results in Ref. [5]. The spatial development of the turbulent kinetic energy $k = (u''_\alpha u''_\alpha)/2$ is illustrated in Fig. 10. Up to cross sections at approximately $x/D = 3$ the maximum k-values increase. Further downstream the gradient of the averaged streamwise velocity $\partial \overline{u}/\partial y$ decreases, resulting in a diminished production of turbulent energy. Hence, the k-maxima are reduced and their locations move away from the jet axis, i.e., the turbulent energy distribution exhibits a smoother shape.

We turn now to the investigation of the influence of the grid resolution and of the subgrid model on the solution. The method of integration is still based on the AUSM method. Fig. 11 shows the turbulence intensities in several cross sections in the proximity of the channel exit. At $x/D = 0.6$ the distribution still resembles that of the simultaneously performed channel flow. The
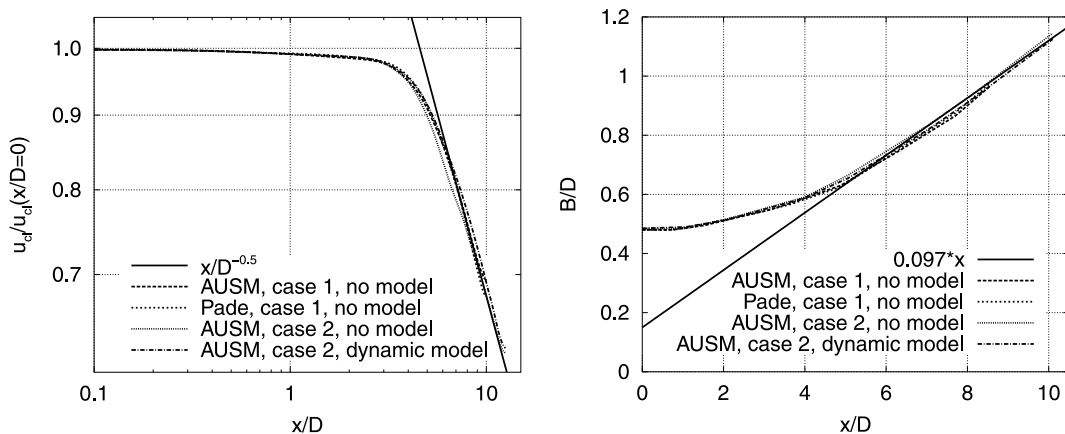
Fig. 8. LES of a turbulent plane jet flow at $Re_D = 7600$ using different solution schemes. Decay of the center-line velocity u_{cl} (left) and the width B/D of the jet vs. x/D (right).
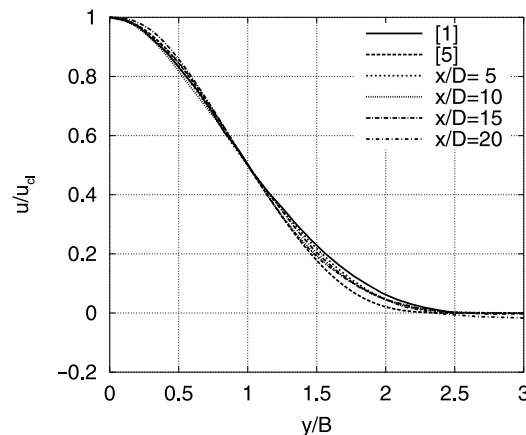
Fig. 9. LES of a turbulent plane jet flow at $Re_D = 7600$ using the AUSM scheme (case 2). Velocity profiles u/u_{cl} vs. y/B at several locations in the streamwise direction x/D.

small discrepancies in the local maxima of the fine and coarse grid solutions become more pronounced in cross sections further downstream. The redistribution process of the turbulence intensities is too slow on the coarse grid. Even when we insert the dynamic subgrid scale model in the coarse grid computation to intensify the energy drain to the small structures, hardly any differences are observed. This confirms the channel flow result, if a second-order accurate method is used the grid resolution has a much larger impact on the statistical variables than the subgrid scale model.

In the following the impact of a high-order discretization on the solution and the efficiency of the method is discussed. For this reason, we juxtapose fine and coarse grid solutions that are computed using the AUSM and the Padé-3/4/6 method with and without a subgrid scale model. The Padé method contains an explicit filtering with $\psi = 0.499$ to ensure a very crisp low pass
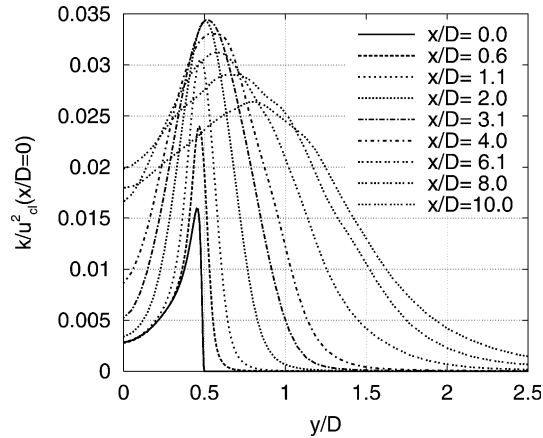
Fig. 10. LES of a turbulent plane jet flow at $Re_D = 7600$ using the AUSM method without subgrid scale model (case 1). Time averaged profiles of the dimensionless turbulent kinetic energy $k/u_{cl}^2(0)$ profiles at different locations x/D.
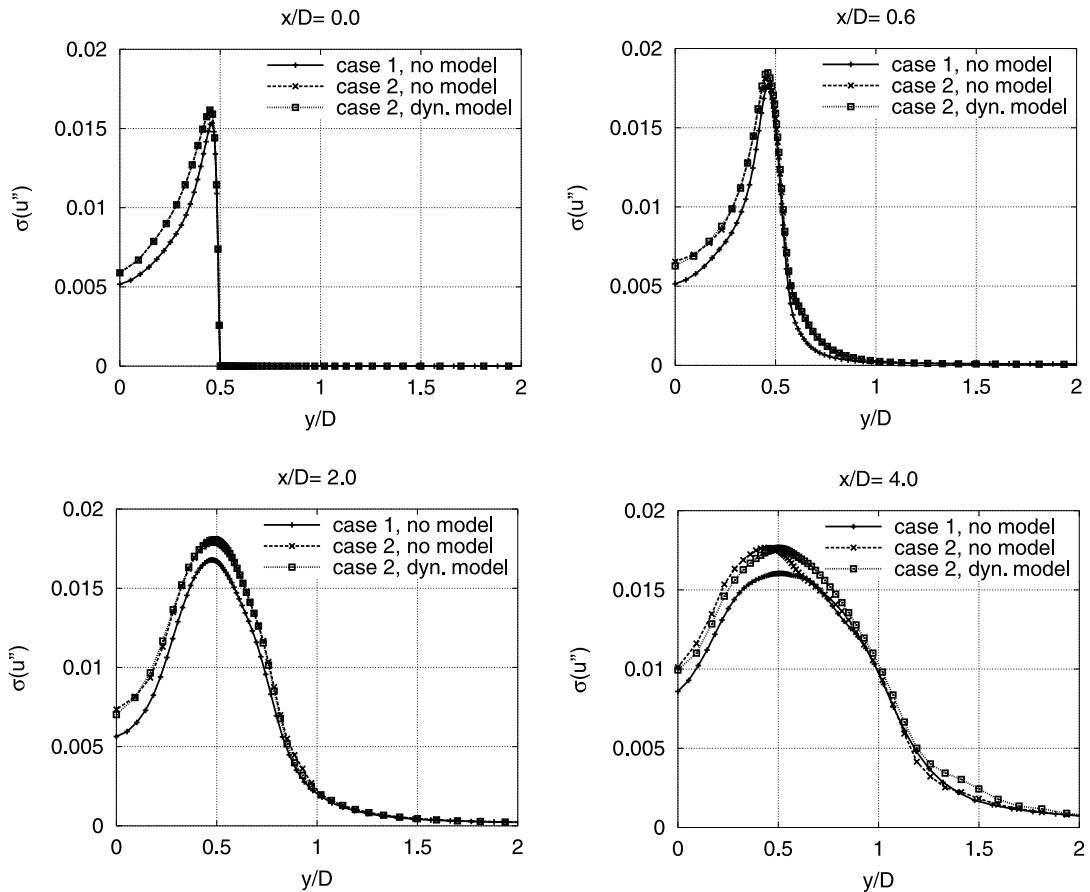

Fig. 11. LES of a turbulent plane jet flow at $Re_D = 7600$ using the AUSM method. Time averaged turbulence intensity profiles $\sigma(u'')$ at different locations x/D.

filtering. As far as the computational effort is concerned, it is approximately 50 percent more costly than the AUSM method. In either case the decrease of the velocity on the jet axis and the spreading rate of the jet in Fig. 8 agree well with the theoretical results. The AUSM and the Padé solution on the fine grid do not exhibit any differences. Also the coarse grid solutions with and without subgrid model almost coincide with the fine grid distributions.

Discrepancies between the various numerical methods and the grid resolutions occur when e.g. the development of the streamwise turbulence intensities $\sigma(u'')$ and the Reynolds stresses $u''v''$ is analyzed (Fig. 12). The Padé findings show strong differences in the fine and coarse mesh solutions. Even the application of the dynamical subgrid model does not diminish the deviations, i.e., although the method is formally sixth-order accurate, the subgrid scale model has hardly any impact on the exchange between the turbulence intensities in the streamwise, wall normal, and spanwise direction. The AUSM data is less sensitive to the grid resolution than the Padé results. In fact, the AUSM findings on the coarse grid without any subgrid model are in much better agreement with the fine grid distributions than the corresponding Padé results using a subgrid scale model. The best correspondence is achieved when $\sigma(u'')$- and $u''v''$-distributions for case 1 are contrasted and neither numerical method contains a subgrid scale model. Only immediately downstream of the channel exit very small differences are observed, that are generated by high-frequency oscillations due to the reduction of the order of accuracy of the Padé method at the jet inflow boundary.

The streamwise turbulence intensities at the Reynolds number $Re_D = 27\,600$ in Fig. 13 show somewhat more clearly what is already indicated in the previous illustrations. The Padé-3/4/6 method generates a slightly smaller maximum and the profiles are a little thicker. The deviations between the AUSM and the Padé method are most pronounced near the inflow boundary where the accuracy of the compact scheme is reduced to third-order. That is, compared with the second-order AUSM scheme the high-order Padé method has no advantage when used on curvilinear meshes. Although a discretization to sixth-order is used, it requires the same grid resolution and the subgrid scale model barely influences the result. Moreover, it is less efficient than the second-order scheme since the computational effort is increased by 150 percent compared with the AUSM method.

5. Conclusion

Two discretization schemes for the large-eddy simulation of turbulent spatially developing jets on body-fitted grids were contrasted. The AUSM based scheme is of second-order accuracy in space, and the compact difference scheme is spatially up to sixth-order accurate. In addition, the impact of subgrid scale models on the quality of the solution was discussed.

The results for a turbulent channel flow showed that the AUSM method produces statistical data in good agreement with direct-numerical and LES results from the literature. The use of a subgrid scale model, however, does not improve the distributions of the statistical variables, regardless of the Reynolds numbers and the grid resolution considered, which is in agreement with results in the literature, where also upwind based methods were applied. The same conclusions can be drawn from the results for the statistical data of the turbulent jet flow.
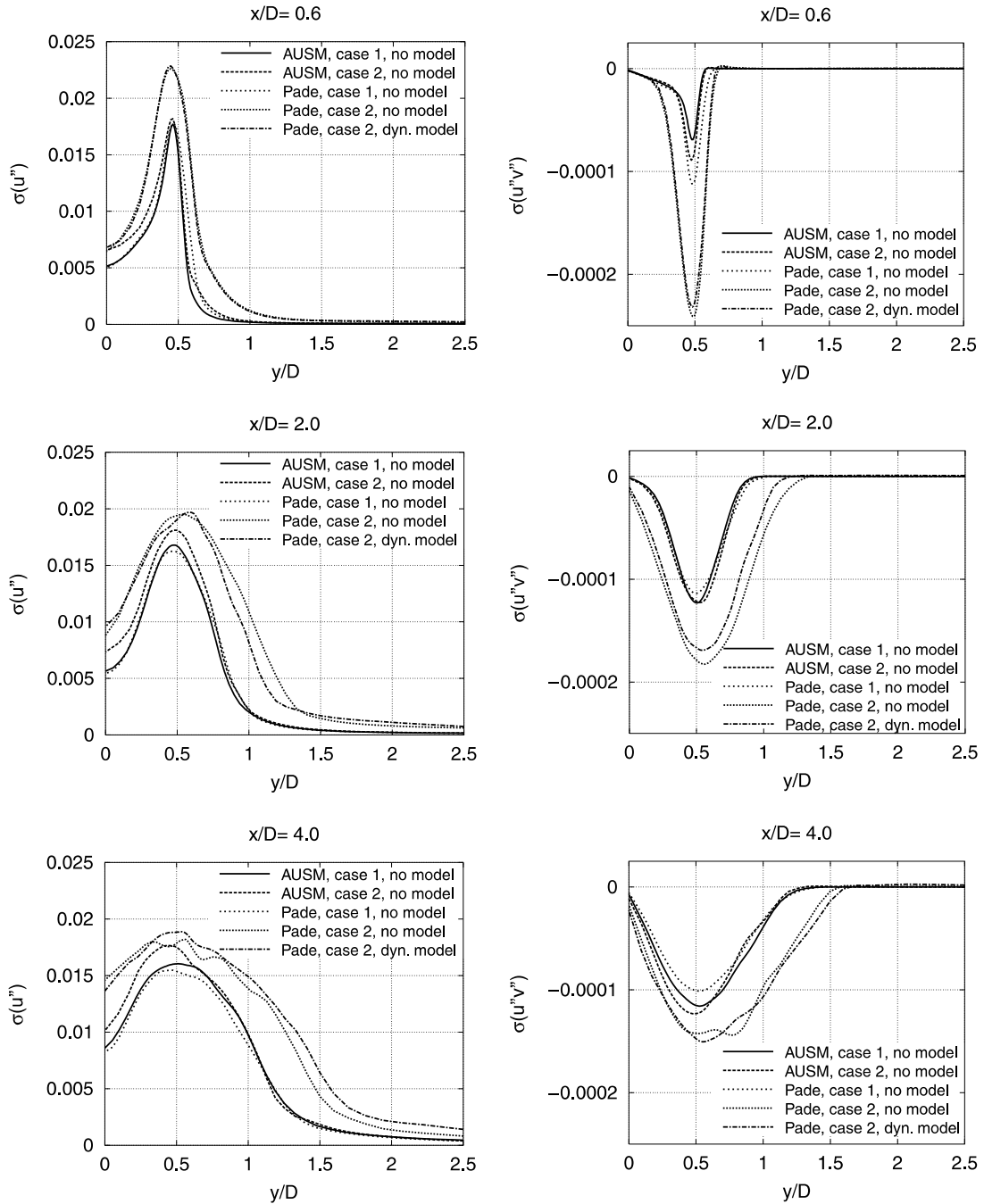
Fig. 12. LES of a turbulent plane jet flow at $Re_D = 7600$. Time averaged profiles of the turbulence intensity $\sigma(u'')$ and the resolved Reynolds stress component $\sigma(u''v'')$ at different locations x/D for the AUSM scheme and the Padé-3/4/6 scheme with $\psi = 0.499$.
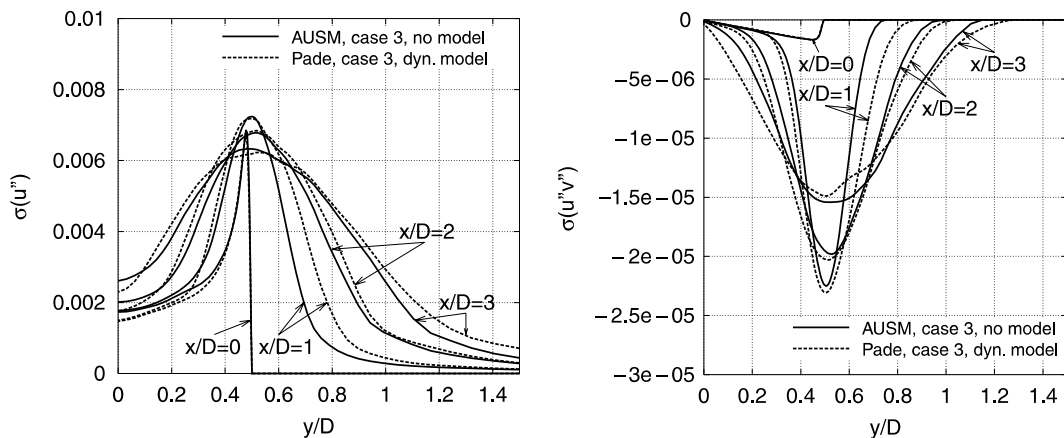
Fig. 13. LES of a turbulent plane jet flow at $Re_D = 27\,600$. Time averaged profiles of the turbulence intensity $\sigma(u'')$ and the resolved Reynolds stress component $\sigma(u''v'')$ at different locations x/D for the AUSM scheme and the Padé-3/4/6 scheme with $\psi = 0.49$.

The LES based on the compact finite difference scheme provides results with an accuracy comparable with that of the AUSM method. The impact of the subgrid scale model on the findings is in the case of the compact scheme also negligible compared to the influence of the mesh resolution or filtering parameters. Although the Padé method is of sixth-order accuracy in the interior of the computational domain, the application of the explicit filtering reduces the high wave number components such that effectively the properties of a solution on a coarser grid are obtained and the benefit of the higher resolution capability in the high wave number range is reduced. The computational effort used for the Padé method is about 150 percent higher than that for the AUSM scheme at the same grid resolution. The statistical data of both schemes is, however, of comparable accuracy. For this reason and due to the good agreement with results from the literature, the AUSM method is considered a sound scheme and, compared to the Padé scheme, the better choice to perform LESs on curvilinear grids.

References

[1] Abramovich GN. In: Schindel LH, editor. The theory of turbulent jets. Cambridge, MA: MIT Press; 1963.
[2] Beaudan P, Moin P. Numerical experiments on the flow past a circular cylinder at sub-critical Reynolds numbers. Technical Report TF-62, Center Turb Res 1994.
[3] Blackwelder RF, Kovasznay LSG. Large-scale motion of turbulent boundary layer during relaminarization. J Fluid Mech 1972;53:61–83.
[4] Blaisdell G, Mansour NN, Reynolds WC. Numerical simulations of compressible homogenous turbulence, Technical Report TF-50. Department of Mechanical Engineering, Stanford University, 1991.
[5] Bradbury LJS. The structure of a self-preserving turbulent plane jet. J Fluid Mech 1965;23:31–64.
[6] Cabot W. Large-eddy simulations with wall models. Ann Res Briefs, Center Turb Res, 1995. p. 41–50.
[7] Choi H, Moin P. Effects of the computational time step on numerical solutions of turbulent flow. J Comput Phys 1994;113:1–4.
[8] Collatz L. Numerische Behandlung von Differentialgleichungen. Berlin: Springer; 1955.

 [9] Dai Y, Kobayashi T, Taniguchi T. Large eddy simulation of plane turbulent jet flow using a new outflow velocity boundary condition. JSME Series B 1994;37(2):242–53.
[10] Eidson TM. Numerical simulation of the turbulent Rayleigh–Benard problem using subgrid modelling. J Fluid Mech 1985;158:245–68.
[11] El Hak MG, Hussain AKMF. Coherent structures in a turbulent boundary layer. Part I: generation of artificial bursts. Phys Fluids 1986;29(7):2124–39.
[12] Erlebacher G, Hussaini MY, Speziale CG. On the large-eddy simulation of compressible turbulence. In: Morton KW, editor. 12th International Conference on Numerical Methods in Fluid Dynamics. Berlin: Springer; 1990. p. 121–6.
[13] Erlebacher G, Hussaini MY, Speziale CG, Zang TA. Toward the large-eddy simulation of compressible turbulent flows. J Fluid Mech 1992;238:155–85.
[14] Favre A. Equations des gaz turbulents compressibles. Journal de Mécanique 1965;4(3):361–90.
[15] Friehe CA. Vortex shedding from cylinders at low Reynolds numbers. J Fluid Mech 1980;100:237–41.
[16] Germano M, Piomelli U, Moin P, Cabot W. A dynamic subgrid-scale eddy viscosity model. Phys Fluids A 1991;3(7):1760–5.
[17] Ghosal S. Analysis of discretization errors in LES. Ann Res Briefs Center Turb Res. 1995. p. 3–24.
[18] Hussain AK, Reynolds WC. Measurement in fully developed turbulent channel flow. Trans ASME 1975:568–80.
[19] Jameson A, Schmidt W, Turkel E. Numerical solution of the Euler equations by finite volume methods using Runge–Kutta time stepping schemes. Pap 81-1259, AIAA, 1998.
[20] Kim J, Moin P, Moser R. Turbulence statistics in fully developed channel flow at low Reynolds number. J Fluid Mech 1987;177:133–66.
[21] Lee S, Lele SK, Moin P. Eddy shocklets in decaying compressible turbulence. Phys Fluids A 1991;3(4):657–64.
[22] Lele SK. Compact finite difference schemes with spectral-like resolution. J Comput Phys 1992;103:16–42.
[23] Lilly DK. A proposed modification of the Germano subgrid-scale closure method. Phys Fluids A 1992;4(3):633–5.
[24] Liou MS, Steffen Jr. CJ. A new flux splitting scheme. J Comput Phys 1993;107:23–39.
[25] Moin P, Squires K, Cabot W, Lee S. A dynamic subgrid-scale model for compressible turbulence and scalar transport. Phys Fluids A 1991;3(11):2746–57.
[26] Piomelli U. High Reynolds number calculations using the dynamic subgrid-scale stress model. Phys Fluids A 1993;5(6):1484–90.
[27] Poinsot TJ, Lele SK. Boundary conditions for direct simulations of compressible viscous flows. J Comput Phys 1992;101:104–29.
[28] Rister T. Grobstruktursimulation schwach kompressibler turbulenter Freistrahlen—ein Vergleich zweier Lösungsansätze. Diss Aerodyn Inst RWTH Aachen 1998.
[29] Rogallo RS, Moin P. Numerical simulation of turbulent flows. Ann Rev Fluid Mech 1984;16:99–137.
[30] Smagorinsky J. General circulation experiments with the primitive equations. Mon Weather Rev 1963;91(3): 99–164.
[31] Smith CR, Metzler SP. The characteristics of low-speed streaks in the near-wall region of a turbulent boundary layer. J Fluid Mech 1983;129:27–54.
[32] Spyropoulos ET, Blaisdell GA. Evaluation of the dynamic subgrid-scale model for large-eddy simulations of compressible turbulent flows. Pap 95-0355. AIAA, 1995.
[33] Taylor GI. Statistical theory of turbulence. Proc Roy Soc 1935;151:421–78.
[34] Van Leer B. Towards the ultimate conservative difference scheme V. A second-order sequel to Godunov's method. J Comput Phys 1979;32:101–36.
[35] Wei T, Willmarth WW. Reynolds-number effects on the structure of a turbulent channel flow. J Fluid Mech 1989;204:57–95.
[36] Yanwen M, Dexun F. Super compact finite difference method (SCFDM) with arbitrarily high accuracy. Comput Fluid Dyn J 1996;5(2):259–76.